

**Rupture dynamics of flat colloidal films**Phalguni Shah *Department of Physics and Astronomy, Northwestern University, Evanston, Illinois 60208, USA*

Eleanor Ward

*Department of Physics and Astronomy, Northwestern University, Evanston, Illinois 60208, USA  
and Currently at Department of Mathematics, Georgetown University, Washington, DC 20057, USA*

Srishti Arora

*Department of Physics and Astronomy, Northwestern University, Evanston, Illinois 60208, USA  
and Currently at Institute for New Materials, Saarbrücken, Germany*Michelle M. Driscoll \**Department of Physics and Astronomy, Northwestern University, Evanston, Illinois 60208, USA*

(Received 3 September 2022; accepted 24 January 2023; published 10 February 2023)

Here, we report experimental results on the rupture of flat colloidal films over a large range of volume fractions,  $0.00 \leq \phi \leq 0.47$ . The films are formed using a constant fluid volume, ruptured with a needle within a few seconds of formation, and recorded using a high-speed camera. We show that colloidal films rupture in a manner similar to Newtonian fluids, even for high colloidal volume fractions. However, higher-viscosity films made of the same fluid volume show a higher thickness away from the boundary at the time of rupture, possibly due to viscous stresses slowing down the thinning of the film. When allowed to spontaneously rupture instead of manually rupturing right after film formation, the same dense colloidal films show exotic instabilities reminiscent of a wrinkling fabric on the film surface. We hypothesize that these instabilities occur because the film is allowed to thin before rupture, and its thickness may compete with the colloidal particle size. Thus, the film lifetime before rupture has a major role to play in the film rupture dynamics, and the effect of microstructure has dramatic consequences in films that are allowed to spontaneously rupture.

DOI: [10.1103/PhysRevFluids.8.024002](https://doi.org/10.1103/PhysRevFluids.8.024002)**I. INTRODUCTION**

Foams, bubbles, and films are ubiquitous in processes that involve liquid-gas interfaces, ranging from detergents [1], volcanic eruptions [2], and water-borne disease transmission [3]. Fluid films are also a convenient system to study the dynamics of fluids in a two-dimensional geometry. Newtonian bubbles have been studied in detail for several decades [4–10], and their rupture dynamics in the inviscid limit are well understood. For inviscid Newtonian films of constant thickness, Culick [8] derived the rupture speed as

$$u_c = \sqrt{\frac{2\sigma}{\rho h}}. \quad (1)$$

\*michelle.driscoll@northwestern.edu

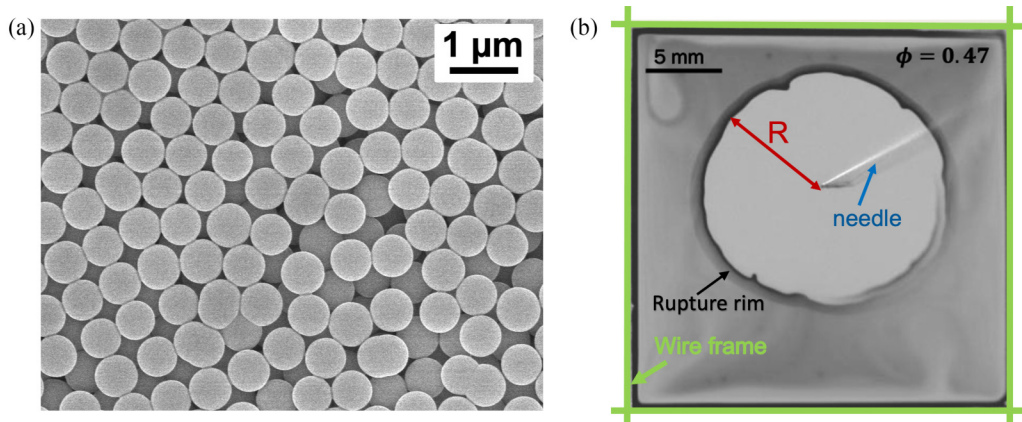


FIG. 1. (a) SEM image of the colloidal silica spheres. The spheres were suspended in the mixture of SDS and water to make suspensions with volume fractions  $0 \leq \phi \leq 0.47$ , and the fluids were used to form horizontal films and record their rupture. (b) A background-divided snapshot of a  $10 \mu\text{l}$ ,  $\phi = 0.47$  film during rupture. After being manually ruptured with a needle, a circular hole forms and its radius,  $R$ , grows until the boundary interferes.

This equation, known as “Culick’s law,” has been experimentally verified for a variety of Newtonian films [5]. In contrast to the linear rupture growth predicted by Culick for low-viscosity films, experiments on higher viscosity liquid curtains have observed a slowing down in rupture growth [11]. Moreover, the rupture of extremely viscous bubbles (a million times more viscous than water) has been observed to grow exponentially [9,10]. Initially, viscoelastic effects were suggested as a cause of this exponential growth, but consequent theoretical work showed that high-viscosity films grow exponentially over a transient timescale directly proportional to fluid viscosity, before asymptotically achieving the Culick velocity [12,13].

A majority of processes involve bursting films that contain surfactants or particulate additives which can significantly alter rupture dynamics. Films with high surfactant concentrations (above the critical micellar concentration) rupture slower than the Culick velocity, and can develop ridges, mesas [14,15], or cracklike instabilities [16]. Films and bubbles composed of smectic materials develop reversible instabilities under stress [17,18] and viscoelastic films display flowering instabilities at the rupture rim [19]. In the ultrathin limit ( $\sim 10 \text{ nm}$ ), even Newtonian soap films exhibit viscoelastic properties that have been attributed to the competing lengthscale of film thickness and the size of surfactant molecules [20]. Films laden with particles larger than film thickness rupture intermittently due to the presence of particles [21]. Thus, both surfactant micelles and particulate additives alter film dynamics significantly, and this effect is more dramatic in the presence of the competing lengthscales of film thickness and additive size.

Here, we report experimental data on the rupture of colloidal soap films over a large range of colloidal volume fraction:  $0 \leq \phi \leq 0.47$ . The silica colloidal spheres used here had a diameter of 660 nm and were synthesized in the laboratory [Fig. 1(a)]. When the colloidal films are ruptured in the center, a circular hole opens and grows with time (Fig. 1(b), see also Supplemental Material (SM) video 1 [22]). We record this rupture with high-speed imaging. Our experiments enable us to access phenomena caused by bulk fluid properties, as well as more striking instabilities. We find that manually ruptured films rupture at a constant speed just like Newtonian films, while thinner and spontaneously rupturing films develop exotic instabilities and rupture in a qualitatively different fashion. We hypothesize that similar to past studies [14–16,20,21], these instabilities may be a result of the particle size being comparable to the film thickness.

For manually ruptured films, the rupture data follows a similar trend as Newtonian films of similar viscosity when plotted in terms of the low-shear viscosity of the colloidal fluid. Our results

demonstrate that rupture dynamics of colloidal films can be characterized using the low-shear viscosity, and additionally that viscosity significantly affects the non-steady-state thickness profile of constant-volume films. This is likely due to viscous stresses in the film slowing down the rate of film thinning. Furthermore, we report exotic instabilities in spontaneously rupturing colloidal films at high  $\phi$ . These instabilities occur in environments of both controlled and uncontrolled humidity, but they are consistently reproducible only in a humidity-controlled environment. We hypothesize that these unstable structures develop when the film thickness is within an order of magnitude of to the colloidal size, as the films are allowed to thin for a longer time in case of spontaneous rupture. This is a convenient system to study suspension dynamics in a quasi-2D geometry, and may help us uncover the transition from continuum dynamics to discrete effects in colloidal fluids. Therefore, films made of the same fluid show strikingly different rupture behavior depending on the time between film formation and time of rupture initiation.

## II. EXPERIMENTAL METHODS

### A. Colloidal synthesis

The silica colloidal spheres were synthesized following the Stöber process [23,24]. To initiate the reaction, we mixed TEOS (tetraethyl orthosilicate) with ethanol and water at room temperature and in presence of ammonia as a catalyst. Subsequently, we added a feed of TEOS and water to increase the particle size. We used the total number of feeds as the means to control particle diameter. The colloids were then washed with ethanol, separated to decrease polydispersity, and resuspended in water. The average silica sphere diameter used for experiments reported here was  $660 \pm 20$  nm [Fig. 1(a)]. The density of the silica particles thus synthesized is 1900–2000 kg/m<sup>3</sup> [24]. Suspensions of volume fractions  $0.00 \leq \phi \leq 0.47$  were prepared in water that contained 4 mM sodium dodecyl sulfate (SDS), a surfactant. The silica particles synthesized using the Stöber process have a negative surface charge, ensuring that particles are suspended in the bulk of the fluid. As the concentration of SDS (measured with respect to the water as opposed to the silica-water suspension) is well below the critical micellar concentration of 8 mM for SDS-water, we do not expect SDS to affect the system in any way other than decreasing the overall surface tension. To compare colloidal rupture data to Newtonian fluid films, we performed rupture experiments on water-glycerol mixtures in the presence of 4 mM SDS, so that the fluid viscosity ranges from 1 to 235 mPa s [25].

### B. Experimental setup

Experiments on film rupture commonly involve spherical bubbles formed from a reservoir [9,10,26] or vertical films [4,5]. However, as evaporation effects are more pronounced for dense colloidal suspensions, the reservoir setup is not convenient for colloidal films. Therefore, in our experiments, we form flat horizontal films by introducing a constant volume of fluid onto a custom film stretcher inspired by past experiments with bacterial films [27].

To form horizontal films of reproducible and controlled thickness, we built a custom film stretcher inspired from Sokolov *et al.* [27] (see also SM video 2 [22]). The stretcher is made of acrylic pieces cut using a laser cutter. On the stretcher base sit two U-shaped components, so that Component 2 fits inside Component 1 [Fig. 2(a)]. Each component has taut nylon-coated steel wires that crisscross to form a small square hole. Component 1 is stationary, while Component 2 is attached to a motor and can be moved horizontally at a constant speed. A known volume of fluid can be introduced on the small square hole formed by the wires. When Component 2 is pulled by a motor, the square hole expands, allowing us to form a horizontal square film of desired size [Fig. 2(b)]. For all experiments reported here, Component 2 was pulled at the speed of 0.8 mm/s. This pulling speed was observed to be optimal for obtaining a stable film of size 25 mm  $\times$  25 mm, and this speed was not varied in the experiments reported here. To minimize the effects of air currents, impurities, and evaporation, the film stretcher was mounted inside a custom humidity chamber and the relative humidity was maintained between 75% and 85% using a reservoir of NaCl

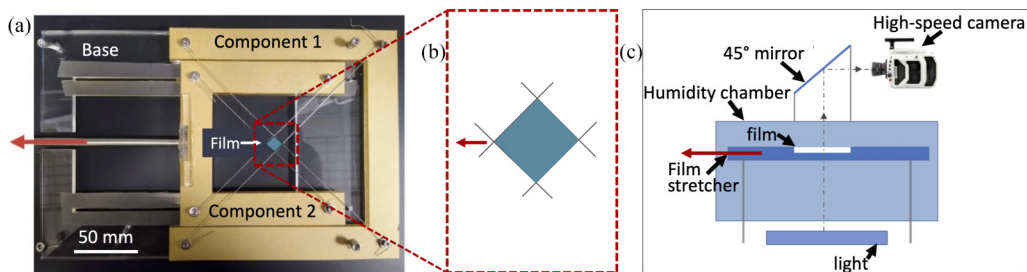


FIG. 2. (a) Top view of the film stretcher designed to make films of a desired size and reproducible thickness (see also SM video 2 [22]). (b) A known volume of fluid is introduced between the crosswires, and then the stretcher is drawn using a motor to expand the crosswires and form a film of desired size. We used the fluid volumes of 10 and 15  $\mu\text{l}$  in our experiments. (c) Side view of the experimental setup. The film stretcher is enclosed in a chamber that maintains relative humidity between 75% and 85% during experiments. The horizontal film is lit from below and its rupture is filmed using a high-speed camera.

solution inside the chamber [Fig. 2(c)]. The film size was 25 mm  $\times$  25 mm, and films were formed using two fluid volumes: 10 and 15  $\mu\text{l}$ . These two fluid volumes were chosen, as these volumes are large enough to form stable films of micron-thickness, while being small enough so that the liquid wets the wire frame, and does not form a drop and fall under its own weight. The horizontal films were illuminated from below using a white panel light and the transmitted light data was recorded at 83 000 fps using a Phantom v2512 high-speed camera. The rupture was manually initiated near the center of the film using a needle within 5 s of film formation [Fig. 1(b)]. For the viscous film rupture data, we made solutions with known concentrations of glycerol and water by mass, and used a constant SDS concentration of 4 mM in all the mixtures. These Newtonian films were also formed using the same film stretcher, and with fluid volumes of 10 and 15  $\mu\text{l}$ .

### C. Film profile characterization

To compare film thickness profiles for films of different fluid viscosities, we used two different techniques: interference imaging and dye absorbance. For the interference imaging, a green filter of wavelength  $530 \pm 10$  nm was introduced in the path of the light, and films of two different viscosities were imaged before rupture was initiated. For the dye absorption measurements, we dissolved 10 g/l of Brilliant Blue dye (Erioglaucine disodium salt) in the mixtures that contained varying amounts of glycerol and water, in presence of 4 mM SDS. As the presence of dye does not change the surface tension of water [28], the surface tension of the mixture is determined by accounting for the presence of glycerol and SDS. We imaged these dyed films under transmitted white light, using the same high-speed camera as the one used to collect the rupture velocity data.

### D. Data analysis

Image processing and analysis were performed using ImageJ, and data was plotted using python. To measure the rupture velocity, the frame of rupture initiation was identified, and the distance from the initiation point to the rupture rim was measured for every 10th frame, until boundary conditions affect the rupture, approximately when rupture radius is around 10 mm (for the wire frame size of 25 mm). The dye absorbance images were background-normalized with the last frame of the image sequence, where the film was absent due to completion of rupture. A rectangular region, 10 pixels in height and the length of the film in width, was selected near the film center, and the line profile, averaged over the 10 pixels, was plotted. This procedure was repeated for different viscosity films.

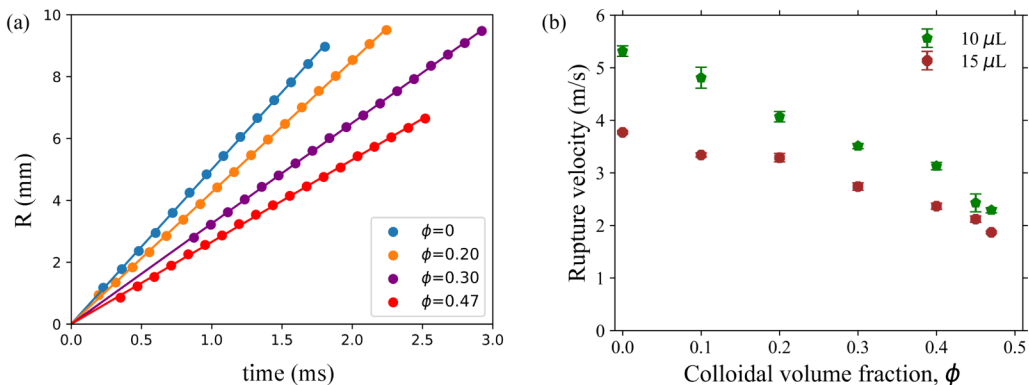


FIG. 3. (a) Rupture radius vs time for  $15 \mu\text{L}$  films made of fluids with increasing colloidal volume fraction  $\phi$ . The rupture velocity (slope of the linear fit lines) is surprisingly constant even at  $\phi$  where the fluid is highly non-Newtonian. (b) The film rupture velocity, plotted against  $\phi$  for two fluid volumes, decreases with increasing  $\phi$ . Error bars are standard deviations over at least five trials.

### III. RESULTS AND DISCUSSION

#### A. Rupture velocity: Colloidal versus viscous Newtonian films

Figure 1(b) shows a snapshot of a colloidal film mid-rupture. When the rupture is induced in the center of the film, a circular hole forms in the film and grows in size. We measure the radius of this hole,  $R$ , with respect to time,  $t$ , for suspension films of increasing  $\phi$ . In Fig. 3(a), we report this data, truncated at the point in time when the effect of film boundary destroys the circular symmetry of the rupture (when the rupture radius is about 10 mm). Surprisingly, even at very high  $\phi$  where the bulk colloidal suspension is known to be highly non-Newtonian, the  $R$  versus  $t$  data follows a linear trend indicating a constant rupture velocity over time. The lines in Fig. 3(a) indicate linear fits to the  $R$  versus  $t$  data, and their slope is the rupture velocity. Though it remains constant throughout rupture, the rupture velocity systematically decreases with increasing  $\phi$ , for both fluid volumes [Fig. 3(b)].

The observation of a constant rupture velocity similar to Culick's law, even at high  $\phi$ , indicating that the rupture of colloidal films may still be modeled as that of a Newtonian fluid. The well-known picture of Newtonian film rupture is that the rim at the rupture boundary collects more and more fluid as it rolls outward. In other words, the rupture does not affect most of the film outside the rupture, except for a small region around the rupture rim referred to as an aureole [5]. Thus, it is expected that no shear is experienced by the film outside of the aureole. Therefore, our observation that the non-Newtonian rheology has a minimal effect on the rupture, even at high values of  $\phi$ , is consistent with this mechanism. In addition to introducing non-Newtonian flow behavior, adding colloidal particles increases the Newtonian viscosity of the fluid [29,30] even in the zero-shear limit. To compare the rupture of colloidal films to its Newtonian counterpart, we used the low-shear viscosity of suspensions measured via cone-plate rheology (see SM for rheology data). We note that there are several models for predicting suspension viscosity in this limit, and using one of these models instead of experimental viscosity measurements does not alter our conclusions.

In Fig. 4, we plotted the film rupture velocity, normalized with respect to  $\phi = 0$  (soap-water film), against this low-shear viscosity. Plotted on the same graph is the rupture data of viscous glycerol-water films using the same experimental setup. Both datasets show a similar decreasing trend in normalized rupture velocity. The agreement between these datasets verifies that due to the shear-free conditions in this system, the low-shear viscosity of the suspension is the dominant parameter that controls the rupture velocity. We note that while the rupture velocity is constant as predicted by Culick, the magnitude of the rupture velocity decreases with increasing fluid viscosity. Theoretical work has predicted Culick's law to hold even for viscous films after a short initial

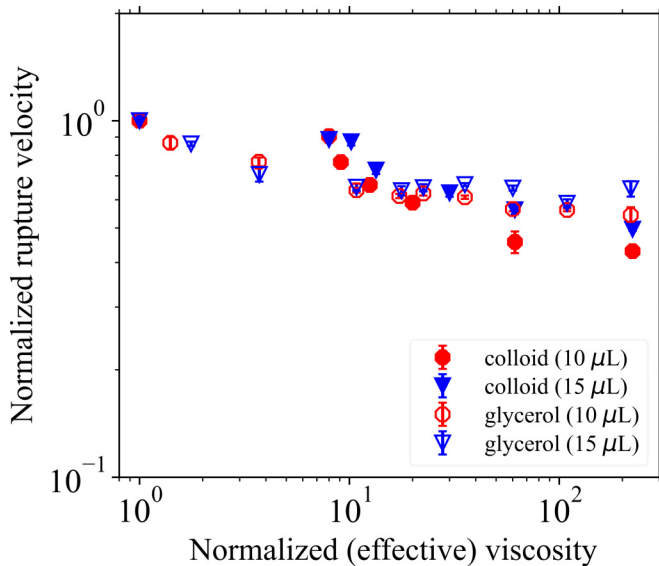


FIG. 4. Rupture velocity of colloidal films plotted against the low-shear viscosity, along with Rupture velocity of Newtonian (glycerol-water) films plotted against fluid viscosity, for two fluid volumes. Both colloidal and Newtonian rupture follow a similar decreasing trend on a log-log plot, indicating that low-shear viscosity is a useful parameter to interpret rupture of colloidal films.

transient, on a timescale  $t_{\text{vis}} = \frac{\eta H}{2\sigma}$  [12,13]. For the fluids considered here, this transient is shorter than the temporal resolution of our experiments ( $\leq 10 \mu\text{s}$ ). As the film is expected to rupture at the Culick velocity after this transient, the decrease in rupture velocity may be attributed to an increase in film thickness for more viscous films, even though we formed our films with the same fluid volume.

### B. Film thickness estimation

Theoretical studies have shown that viscous films rupture at the same speed as Culick velocity, after a brief transient of a timescale that depends on viscosity [12,13]. For the experimental conditions in this study, this transient is smaller than the temporal resolution of our high-speed camera ( $\leq 10 \mu\text{s}$ ). Therefore, according to this model, we should still observe rupture dynamics that follow Culick's law, and the rupture velocity of constant-thickness films should be independent of fluid viscosity. Our observations of decreasing rupture velocity [Fig. 3(b)] with increasing viscosity are clearly in contradiction with this. To explore whether this decrease is attributable to an increase in film thickness, we characterize the film thickness as a function of fluid viscosity. The refractive index mismatch between colloidal particles and the suspending fluid poses a challenge in characterizing film thickness using interferometry or dye measurements. Therefore, we carry out these measurements for Newtonian glycerol-water films.

The side length of the square films formed in our experiments is  $L_{\text{film}} = 25 \text{ mm}$ . Using the two fluid volumes from our experiments and assuming a perfectly flat film, volume conservation allows us to estimate the film thicknesses as

$$h_{10} = \frac{10 \mu\text{l}}{L_{\text{film}}^2} = 16 \mu\text{m}, \quad (2)$$

and

$$h_{15} = \frac{15 \mu\text{l}}{L_{\text{film}}^2} = 24 \mu\text{m}. \quad (3)$$

We note that these values are upper bounds on the true film thicknesses. A more accurate estimate of the true thickness away from film boundary can be made for inviscid soap-water films, using our rupture velocity data and Culick's law:

$$h_{10,c} = \frac{2\sigma}{\rho v_{10,c}^2} = 3.2 \mu\text{m} \quad (4)$$

and

$$h_{15,c} = \frac{2\sigma}{\rho v_{15,c}^2} = 6.2 \mu\text{m}, \quad (5)$$

where  $\sigma$  is the surface tension of 4 mM SDS in water (45 mN/m),  $\rho$  is the density of water (1000 kg/m<sup>3</sup>), and  $v_{10(15),c}$  is the rupture velocity from our experimental data for 10(15)  $\mu\text{l}$  films. We note that for glycerol-water mixtures, the fluid density is increased (for glycerol concentration ranging from 0% to 95% in our experiments,  $1000 \text{ kg/m}^3 \leq \rho_{\text{fluid}} \leq 1250 \text{ kg/m}^3$ ). Accounting for this density difference would further decrease the film thickness estimates in Eqs. (4) and (5). Thus, the thickness estimated using the Culick velocity is much smaller than the volume conservation estimate, indicating that the films formed in our experiments are not perfectly flat.

Interferometry is commonly used to characterize the thickness profile of thin fluid films [31]. Figure 5 shows images of films made from the same fluid volume (15  $\mu\text{l}$ ), but with fluids of different viscosities under a narrow-width bandpass filter ( $\lambda = 530 \pm 10 \text{ nm}$ ). The fluid viscosity of the film imaged in Fig. 5(a) is  $\eta = 2 \text{ mPa s}$ , and that showed in Fig. 5(b) is  $\eta = 35 \text{ mPa s}$ . While the 2 mPa s film shows distinctive interference fringes, fringes are largely absent for the 35 mPa s film, except near the film boundary. The absence of fringes in Fig. 5(b) indicate that the film thickness away from the boundary is larger than the coherence length for the bandpass filter used. The coherence length can be calculated as

$$l_c = C \frac{\lambda^2}{n\Delta\lambda}, \quad (6)$$

where  $n$  is the refractive index of the medium (calculated for every film composition using the refractive index of 1.33 for water and 1.45 for glycerol) and  $C = 0.44$  [32]; For  $\lambda = 530 \text{ nm}$  and  $\Delta\lambda = 10 \text{ nm}$ , we obtain  $l_c = 9.3 \mu\text{m}$ . Thus, we infer that the higher-viscosity (35 mPa s) film is thicker than the low-viscosity (2 mPa s) film, despite being made of the same volume of fluid. As thicker films rupture at lower speeds according to Culick's law, this is also consistent with the lower rupture speed we observed for viscous films. Additionally, in Fig. 5(b), we observe an interference pattern near the film edge, although fringes are absent near the middle. This suggests that the film has a nonmonotonic thickness profile. To characterize this film thickness profile in more detail, we collect dye absorbance data for films of varying viscosity.

Figures 5(c) and 5(d) show images of fluid films of viscosities 1 and 100 mPa s, respectively, containing 10 g/l Brilliant Blue dye and imaged under white light. For dyed fluids, the absorbance gives the fraction of light absorbed by the sample and is calculated as

$$\text{Absorbance} = 1 - \text{normalized intensity of transmitted light}.$$

Figure 5(e) shows a plot of absorbance for both films, across a line drawn through the center of the film. To minimize noise, the profile averaged over a 10-pixel wide box around the line is plotted. As a thicker sample absorbs more light, the absorbance profile qualitatively captures the features of the film thickness profile. The more viscous film (blue line) shows a higher absorbance near the film

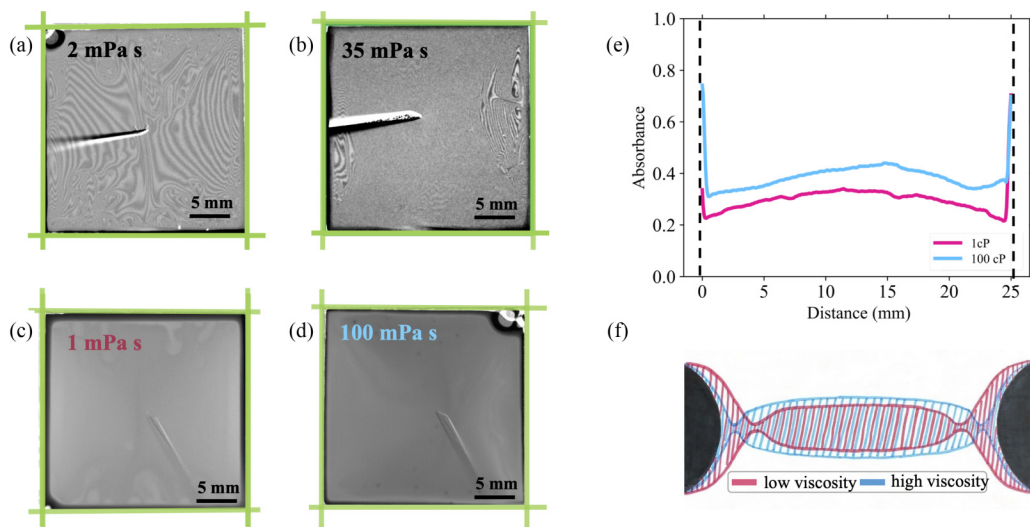


FIG. 5. (a) Interference fringes observed under a green filter ( $\lambda = 510 \pm 10$  nm) for a low-viscosity film (2 mPa s), and (b) a higher-viscosity film (35 mPa s). The change in the interference pattern indicates that the thickness profile changes with fluid viscosity. (c), (d) 15  $\mu$ l Newtonian films of viscosities **c** 1 mPa s and **d** 100 mPa s, containing Brilliant Blue dye. The films transmit different amounts of light, indicating a different film thickness. (e) Absorbance of both the films plotted along a line going through the center of the film. Higher absorbance indicates higher film thickness, thus the film thickness profile is proportional to the absorbance profile. (f) Schematic showing the hypothesized variation in thickness profile with increasing viscosity. The pink shaded area indicates a lower-viscosity film, and the blue indicates a higher viscosity film made of the same fluid volume. The length of the meniscus near the film edge is smaller for a more viscous film, and so is the location where film thickness is minimum. Away from the boundary, both films assume a flat, practically constant-thickness shape, with the more viscous fluid forming a thicker film. Features are exaggerated for clarity.

center, further evidence that more viscous films lead to thicker films despite being made from the same fluid volume.

Two other features of the absorbance profile are informative. First, the absorbance increases rapidly near the film boundary, indicating a drastic increase in film thickness. This can also be observed in the Figs. 5(c) and 5(d), in the form of a darker region near the wire frame, corresponding to this thicker meniscus. The second interesting feature is that the absorbance reaches its minimum as we move toward the center of the film from the meniscus, well before the film assumes a relatively flat shape. The thinnest part of the film is therefore located next to the meniscus near the boundary, and not near the center of the film. Quantifying film thickness with dye absorbance data is difficult, as making calibration samples as thin as a few microns is experimentally challenging. Nevertheless, the qualitative features of the absorbance profile allow us to construct a sketch of the film thickness profile.

Figure 5(f) shows a sketch of the thickness profile inferred from our interferometry and dye absorbance measurements, as seen from the side. This is a schematic, and features are exaggerated for clarity. Films have a large thickness (of the order of the wire frame thickness) near the boundary, which dramatically decreases as we move away from the boundary. The thickness reaches a minimum before rising again, and achieves a relatively flat profile near the center. The more viscous film (blue shaded region) is thicker in the middle than the low-viscosity film (pink shaded region), leading to a slower film rupture (Fig. 4). This occurs because the meniscus near the film edge can be made of different fluid volumes. Thus, the area contained by the two schematic profiles is the same, corresponding to films containing the same fluid volume.

As the thickness of the wire frame (500 microns) is much larger than the average film thickness near the center (a few microns), we can compare our system to a fluid film attached to a flat “plateau border” [33–36]. In this case, the pressure difference between the fluid near the film center and near the film boundary causes an outward fluid flow and a wider fluid meniscus near the boundary. If we assume film surfaces to move in a stress-free manner, then the film thickness decreases monotonically from the boundary to film center [36]. On the other extreme, the assumption of a perfectly immobile film surface leads to a thickness minima between the thicker meniscus and the film center. The reality is between these two extremes, i.e., flow is present along film surface, accompanied by Marangoni stresses. Thus, experimentally studied films may show this thickness minima near the boundary, just as we observe in our experiments and the sketch in Fig. 5(f). This minima is also related to the “marginal regeneration” phenomenon first reported by Mysels, Shinoda, and Frankel [4]. Such patches of minimal thickness have been observed for both vertical [34] and horizontal [37] films, and in 1-dimensional models of fluid films [38]. From our rupture data (Fig. 4) and thickness profile characterization [Figs. 5(e) and 5(f)], we can infer that the location of the minimal thickness ‘pinches’ right before rupture differs as a function of fluid viscosity. As we rupture the film within a few seconds of stretching, the film profile is not in steady-state. Past theoretical work has shown that for a horizontal film attached to a thicker meniscus at the boundary, the rate of plane-parallel thinning is slowed down due to viscous stresses in the film [39]. We believe our observations are capturing just this phenomenon: for a more viscous film, the fluid drains more slowly from the film center into the meniscus, causing a narrower meniscus near the edge and a thicker film near the center right after film formation [Fig. 5(f)]. This thicker film in turn causes a slower rupture speed.

Thus, our characterization of the film thickness profile indicates that when a constant volume of fluid is used to make horizontal flat films, the non-steady-state film thickness profile right after film formation—and in turn the film thickness away from the boundary—varies fluid viscosity, as viscous stresses slow down the plane-parallel thinning of the film. Consequently, the film thickness affects the rupture velocity. Our results are consistent with past predictions [12,13] that Culick’s law is asymptotically applicable even for the rupture of viscous films. Using equation 1, we convert the rupture velocity into film thickness:  $h = \frac{2\sigma}{\rho v^2}$ . Figure 6 shows the thickness thus calculated plotted against the fluid viscosity (for colloidal data, low-shear viscosity), showing an increasing trend in film thickness with viscosity. We note that the Newtonian and colloidal data begin to diverge for higher fluid viscosities; this may be attributed to non-Newtonian effects in colloidal films at higher  $\phi$ , in addition to the low-shear viscosity. The dotted lines indicate the upper-bound film thickness estimated from volume conservation, Eqs. (2) and (3). Quantitative comparison with models of viscous thinning could not be made, since unlike model systems, our experimental system has a constant-volume constraint that may significantly affect thinning dynamics.

### C. Instabilities in spontaneously rupturing colloidal films

In contrast to films manually ruptured near the center, when constant-volume colloidal films were allowed to rupture spontaneously, we observed instabilities developing and propagating into the intact film during rupture (Fig. 7, SM videos 3, 4, and 5 [22]). Spontaneous rupture always happened near the film edge; the instabilities were almost nonexistent when similarly prepared films were manually ruptured away from the boundary. Our qualitative characterization of the film thickness profile [Figs. 5(e) and 5(f)] suggests that the film is thinnest near the edge, between the thicker meniscus near the wire frame and the approximately flat film near the center [Fig. 5(f)]. Thus, our observation that spontaneous rupture always occurs near the edge is consistent with the film thickness profile.

For the experiments where we observed instabilities, we formed colloidal fluid films of about 12 mm in size with 2  $\mu$ l of fluid, and recorded the film until it spontaneously ruptured. We observed instabilities in experiments where humidity was not controlled for [Figs. 7(a) and 7(b)], and also in controlled humidity experiments inside the humidity chamber (Figs. 7(c) and 7(d), SM video 5 [22]).

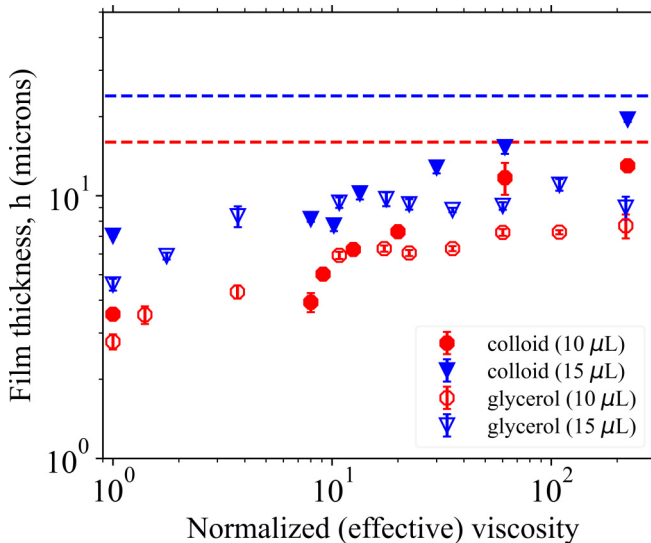


FIG. 6. Film thickness, calculated using Culick’s law, plotted for both Newtonian and colloidal films. For both viscous and colloidal fluids, the film thickness increases with increasing fluid viscosity, consistent with the interferometry and dye absorbance observations. Dotted lines indicate the upper bound in film thickness for each fluid volume, estimated by volume conservation.

Figures 7(a) and 7(b) show  $\phi = 0.35$  colloidal films, where the suspending fluid is 2 mM SDS in 30% glycerol and 70% water, rupturing at ambient humidity ( $RH \sim 30\%$ ). We note that these experiments were done using an earlier version of the setup where films were made using an expandable camera iris, leading to a quasi-circular film geometry. Scale bars in all panels are 2 mm. We note that the films in Figs. 7(a) and 7(b) were made of the same fluid, and yet they showed drastically different patterns during rupture. Additionally, the rupture time of the two films differed by a factor of 3. This lack of reproducibility may be attributed to large fluctuations in the ambient humidity.

Figures 7(c) and 7(d) show 12 mm square films with  $\phi = 0.40$  in 4 mM SDS and water, rupturing under controlled humidity ( $RH = 80\%$ ). Once again, the rupture begins near the edge and instabilities propagating throughout the film. A thicker (darker) structure forms in the intact film, and then the rest of the film appears to wrinkle like a fabric around this thicker filament. After rupture, we observe the filament to flow like a fluid, indicating that evaporation has not dried out the film (see also SM video 5 [22]). In these humidity-controlled experiments, both the qualitative rupture behavior and the rupture time were reproducible over multiple trials. Thus, controlling the ambient humidity and in turn evaporation is important to obtain qualitatively reproducible instabilities.

The instabilities had several striking features. In the beginning of rupture, the rupture boundary is jagged as opposed to the smooth rupture boundaries for manually ruptured films. The manually induced rupture rim rolls outward smoothly, while the spontaneous rupture with instabilities is similar to an elastic sheet depinning from the wire frame. The instabilities are reminiscent of folds or wrinkles on a fabric. Even for controlled humidity, the significant variation in the shape of the rupture front and the location of instabilities makes quantifying their dynamics a challenge. The lack of reproducibility in the rupture dynamics in case of uncontrolled humidity might be a result of the significant amount of stochasticity due to fluctuating humidity and ambient impurities.

We observe these instabilities only for a specific set of conditions. They occurred at high values of colloidal  $\phi$ , and for relatively thinner films. For films in Figs. 7(c) and 7(d), volume conservation estimate with  $L_{\text{film}} = 12$  mm and fluid volume of 2  $\mu\text{l}$  leads to  $h = 12$   $\mu\text{m}$ , smaller than the estimate in Eq. (2). We note that this is the upper bound for film thickness, and the meniscus near the film

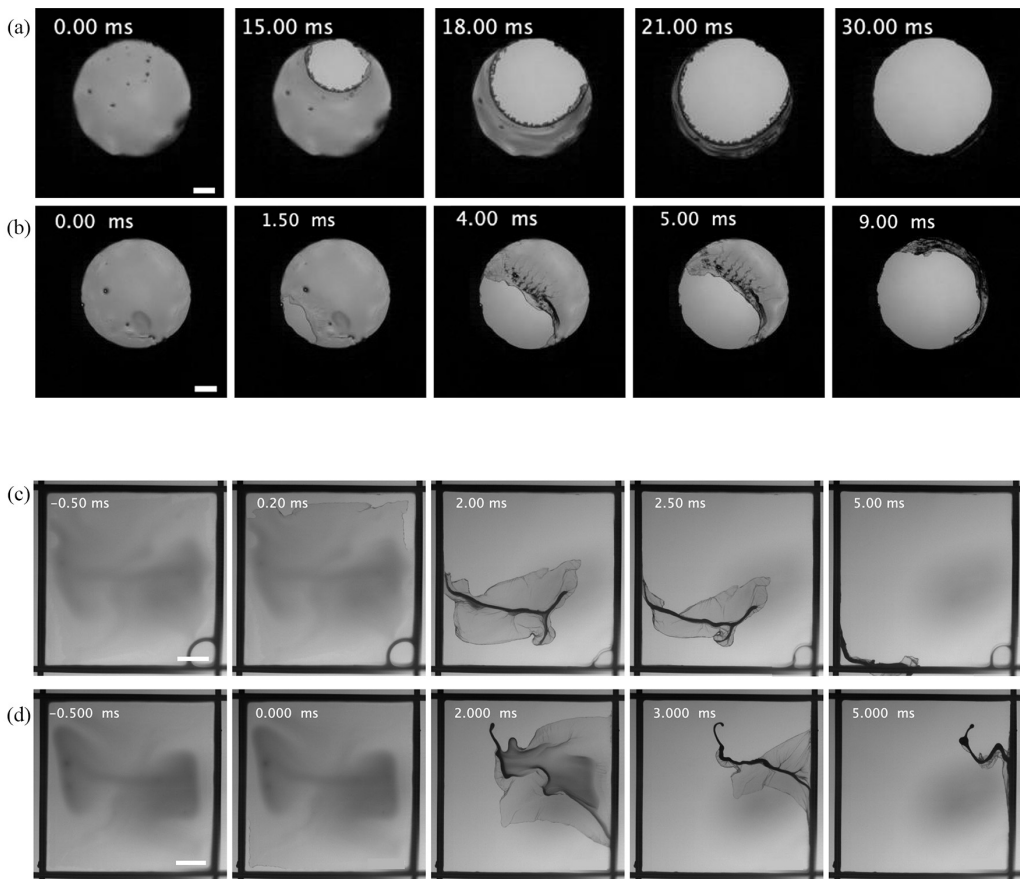


FIG. 7. (a), (b) Instabilities develop in spontaneously rupturing colloidal films at low humidity ( $RH \sim 30\%$ ). The film composition is  $\phi = 0.35$  colloidal particles, where the suspending fluid is 2 mM SDS in 30% glycerol and 70% water. In uncontrolled humidity, instabilities are not reproducible (see also SM videos 3 and 4 [22]). (c), (d) Instabilities also develop in spontaneously rupturing colloidal films at high humidity ( $RH > 75\%$ ). The film was made of fluid with  $\phi = 0.40$  colloids in 4 mM SDS and water (see also SM video 5 [22]). In a humidity-controlled environment, instabilities are much more reproducible. Scale bars are 2 mm.

boundary leads to a much thinner film near the center, as demonstrated by Eq. (4). Thus, we expect the films in Figs. 7(c) and 7(d) to be thinner than the  $3.2 \mu\text{m}$  estimate in Eq. (4), making them only a few times thicker than the 660 nm silica particles. For films to spontaneously rupture, we waited for rupture after forming the film. Over this waiting time, the film could have thinned further. We therefore hypothesize that these structures develop when the colloidal size (660 nm) competes with the film thickness (a few microns).

Although the nontrivial geometry of the rupturing film made it challenging to measure the rupture speed, we can estimate the rupture speed using the film side length (12 mm) and time of rupture (7 ms),  $v_{\text{rupture}} = 1.7 \text{ m/s}$ . If the rupture were to follow Culick's law, then this rupture speed would correspond to a  $22 \mu\text{m}$  film. This is clearly unphysical, as this thickness is above the upper bound of thickness estimated using volume conservation,  $13 \mu\text{m}$ . Therefore, instabilities significantly slow down rupture. In other systems, such a slowing down has been attributed to film elasticity [16]. A deeper investigation into the cause of these modified film dynamics would provide more information about the microscopic dynamics in colloidal films.

Extremely viscous liquids also show buckling instabilities under compression [40,41], and a “parachute instability” in punctured viscous films has recently been attributed to viscous bending similar to that seen in elastic sheets [42]. The fluid viscosities in these studies are much larger than the viscosity range explored in the experiments reported here. Another recent study has reported foldlike instabilities in collapsing Newtonian films, when rupture was initiated at the film boundary [43]. The origin of these folds was attributed to the geometric singularity caused by the sharp corners of the frame, as folds were absent in a smoother frame geometry. Thus, the initiation of the rupture near the square frame in our spontaneous rupture experiments may also contribute to the occurrence of these instabilities. As seen from the lack of reproducibility in ambient low humidity, evaporation seems to affect the time of rupture and nature of instabilities, possibly by introducing additional surface stresses. We expect the evaporation effect to be especially high in films with high colloidal  $\phi$  and lower thicknesses due to the high surface area of the film. Future studies systematically investigating the effects of humidity and film geometry on instabilities would be informative. Highly controlled future experiments may enable a more quantitative characterization of the instabilities, and enrich our understanding of dynamics of suspension in a quasi-2D geometry.

#### IV. CONCLUSION

Here, we report the rupture velocity data of flat colloidal films in the range of volume fractions  $0 \leq \phi \leq 0.47$ , and of glycerol-water films with viscosities 1–235 mPa s. We use a custom film stretcher to make films of two constant fluid volumes, 10 and 15  $\mu\text{l}$ . We observe constant rupture velocity even at high colloidal volume fractions which, when plotted against the low-shear viscosity of the suspensions, agrees well with that of Newtonian glycerol-water films in the same viscosity range. Therefore, even at high  $\phi$  where highly non-Newtonian flow behavior is apparent from bulk rheology, the suspension viscosity at low shear is sufficient to capture the dynamics of colloidal film rupture. As the well-accepted picture of Newtonian film rupture is that the rupture rolls outward collecting fluid, high shear must not be present outside of the film aureole during rupture, despite the short timescale of rupture. Our results demonstrate that rupturing particulate films can be effectively modeled as viscous fluids.

For both colloidal and Newtonian fluids, we observed the rupture velocity of constant-volume films decreases with increasing fluid (low-shear) viscosity. Our characterization of the film thickness profile via interference imaging and dye absorption shows that higher viscosity films lead to higher thickness near the film center, as viscosity modifies the thickness profile at rupture. We reiterate that the films are ruptured within 5 s of formation and the thickness profile has not reached steady state. The difference in these non-steady-state thickness profile may be a result of slower film thinning due to viscous stresses [39].

Although Culick’s derivation of rupture velocity neglected viscous effects, Culick’s law has been predicted to asymptotically hold for high-viscosity fluids [13]. Viscosity is only expected to introduce a transient at the initial stage of rupture, on a timescale  $t_{\text{vis}} = \frac{\eta H}{2\sigma}$ . For our experiments,  $t_{\text{vis}} \leq 10 \mu\text{s}$ , which cannot be observed at the temporal resolution of our experiments ( $\sim 10 \mu\text{s}$ ). Thus, the change in the thickness profile is solely responsible for the slower rupture of more viscous films. A surprising feature of the horizontal film thickness profile is that the film reaches a minimum thickness near the thicker meniscus by the wire frame, away from the film center. This “pinch” in film thickness is reminiscent of the well-known marginal regeneration phenomenon, where the nonmonotonicity in film profile is a direct result of surface stresses in the film [4,36]. This further supports the possibility that viscous stresses have a role in the rate of film thinning and the formation of a pinch in the film thickness profile.

When allowed to rupture spontaneously, flat colloidal films with  $\phi \geq 0.40$  developed exotic instabilities originating at the rupture rim and propagating through the film surface. Films always spontaneously ruptured near the edge. Both the pattern of instabilities and the rupture time were reproducible under controlled and high humidity, while they were much more stochastic when humidity was not controlled for. We hypothesize that these structures occur when the colloidal

size is comparable to the film thickness. Rupturing films are reminiscent of wrinkling fabrics, and instabilities seem to slow down film rupture significantly as compared to the Culick prediction. Other studies have reported instabilities in surfactant films of varying thicknesses above the critical micellar concentration, which have been attributed to the rigidity imparted to the film [16] and to micelles forming mesalike structures [14,15]. Some work has also focused on particulate rafts with  $>100\ \mu\text{m}$  particles, so that the raft is made of small capillary bridges between these particles [21]. However, there are no other works that have considered colloidal-size particles in films that are comparable in size or slightly thicker than the particle, to the best of our knowledge. Film rupture in this parameter regime is a convenient way to study the physics of suspensions in two dimensions. A detailed characterization of this state of the film before it refluidizes after rupture would be a fascinating avenue of future exploration.

While manual rupture was initiated at the film center, spontaneous rupture always occurred near the film boundary. A past work has seen foldlike instabilities even for Newtonian films rupturing near the edge. Thus, the rupture geometry may have a major effect on the presence and propagation of instabilities. Furthermore, we observed instabilities in the rupturing films when we formed the films and waited until rupture happened spontaneously. On the other hand, the manual rupture was initiated within a few seconds of forming the film. This difference in film lifetime likely resulted in thinner films at the time of rupture when we observed instabilities. Thus, varying the lifetime of the film before rupture affects the rupture process greatly.

Our experiments on colloidal film rupture demonstrate that our understanding of Newtonian film rupture can be extended to the rupture dynamics of non-Newtonian films, well into the high volume fraction regime. Despite colloidal film dynamics being surprisingly Newtonian when the films are significantly thicker than particle size, we observed exotic structures in spontaneously rupturing films when the film thickness and particle size were comparable. Further theoretical work aimed toward understanding these discrete effects on the particle scale would greatly enhance our understanding of changes in colloidal microstructure under dynamical conditions in two dimensions. A number of processes such as disease transmission and petrochemical delivery, films and bubbles form and rupture before attaining steady state. We anticipate that our characterization of this non-steady-state profile can inform the control of film rupture in such processes.

#### ACKNOWLEDGMENT

The authors are thankful to Vivek Sharma for useful discussions and insights and the referees for their constructive feedback that significantly improved the discussion presented here.

- 
- [1] E. Kissa, Kinetics and mechanisms of soiling and detergency, in *Detergency* (CRC Press, Boca Raton, FL, 2020), pp. 193–331.
  - [2] M. Cassidy, M. Manga, K. Cashman, and O. Bachmann, Controls on explosive-effusive volcanic eruption styles, *Nat. Commun.* **9**, 2839 (2018).
  - [3] L. Bourouiba, The fluid dynamics of disease transmission, *Annu. Rev. Fluid Mech.* **53**, 473 (2021).
  - [4] K. J. Mysels, S. Frankel, and K. Shinoda, *Soap Films: Studies of Their Thinning and a Bibliography* (Pergamon Press, Oxford, UK, 1959).
  - [5] W. R. McEntee and K. J. Mysels, Bursting of soap films. I. An experimental study, *J. Phys. Chem.* **73**, 3018 (1969).
  - [6] S. Frankel and K. J. Mysels, Bursting of soap films. II. Theoretical considerations, *J. Phys. Chem.* **73**, 3028 (1969).
  - [7] G. I. Taylor, The dynamics of thin sheets of fluid. III. Disintegration of fluid sheets, *Proc. R. Soc. London A* **253**, 313 (1959).
  - [8] F. E. Culick, Comments on a ruptured soap film, *J. Appl. Phys.* **31**, 1128 (1960).

- [9] G. Debrégeas, P.-G. de Gennes, and F. Brochard-Wyart, The life and death of “bare” viscous bubbles, *Science* **279**, 1704 (1998).
- [10] G. Debrégeas, P. Martin, and F. Brochard-Wyart, Viscous Bursting of Suspended Films, *Phys. Rev. Lett.* **75**, 3886 (1995).
- [11] A. Mohammad Karim, W. J. Suszynski, L. F. Francis, and M. S. Carvalho, Effect of viscosity on liquid curtain stability, *AIChE J.* **64**, 1448 (2018).
- [12] M. P. Brenner and D. Gueyffier, On the bursting of viscous films, *Phys. Fluids* **11**, 737 (1999).
- [13] N. Savva and J. W. M. Bush, Viscous sheet retraction, *J. Fluid Mech.* **626**, 211 (2009).
- [14] Y. Zhang and V. Sharma, Domain expansion dynamics in stratifying foam films: Experiments, *Soft Matter* **11**, 4408 (2015).
- [15] C. Ochoa, S. Gao, S. Srivastava, and V. Sharma, Foam film stratification studies probe intermicellar interactions, *Proc. Natl. Acad. Sci. USA* **118**, e2024805118 (2021).
- [16] P. Petit, M. Le Merrer, and A.-L. Biance, Holes and cracks in rigid foam films, *J. Fluid Mech.* **774**, R3 (2015).
- [17] F. Müller, U. Kornek, and R. Stannarius, Experimental study of the bursting of inviscid bubbles, *Phys. Rev. E* **75**, 065302(R) (2007).
- [18] A. Missaoui, K. Harth, T. Trittel, C. Klopp, R. Stannarius, and E. Lacaze, Shape instabilities of islands in smectic films under lateral compression, *Soft Matter* **18**, 3193 (2022).
- [19] D. Tamaro, V. C. Suja, A. Kannan, L. D. Gala, E. D. Maio, G. G. Fuller, and P. L. Maffettone, Flowering in bursting bubbles with viscoelastic interfaces, *Proc. Natl. Acad. Sci. USA* **118**, e2105058118 (2021).
- [20] L. J. Evers, S. Y. Shulepov, and G. Frens, Bursting Dynamics of Thin free Liquid Films from Newtonian and Viscoelastic Solutions, *Phys. Rev. Lett.* **79**, 4850 (1997).
- [21] Y. Timounay, E. Lorenceau, and F. Rouyer, Opening and retraction of particulate soap films, *Europhys. Lett.* **111**, 26001 (2015).
- [22] See Supplemental Material at <http://link.aps.org/supplemental/10.1103/PhysRevFluids.8.024002> for rheological measurements and experimental movies.
- [23] W. Stöber, A. Fink, and E. Bohn, Controlled growth of monodisperse silica spheres in the micron size range, *J. Colloid Interface Sci.* **26**, 62 (1968).
- [24] L. Zhang, M. D’Acunzi, M. Kappl, G. K. Auernhammer, D. Vollmer, C. M. van Kats, and A. van Blaaderen, Hollow silica spheres: Synthesis and mechanical properties, *Langmuir* **25**, 2711 (2009).
- [25] M. L. Sheely, Glycerol viscosity tables, *Ind. Eng. Chem.* **24**, 1060 (1932).
- [26] S. Poulain and L. Bourouiba, Biosurfactants Change the Thinning of Contaminated Bubbles at Bacteria-Laden Water Interfaces, *Phys. Rev. Lett.* **121**, 204502 (2018).
- [27] A. Sokolov, M. M. Apodaca, B. A. Grzybowski, and I. S. Aranson, Swimming bacteria power microscopic gears, *Proc. Natl. Acad. Sci. USA* **107**, 969 (2010).
- [28] C. Vernay, Destabilization of liquid sheets of dilute emulsions, Ph.D. thesis, 2015.
- [29] J. Mewis and N. J. Wagner, *Colloidal Suspension Rheology* (Cambridge University Press, Cambridge, UK, 2012).
- [30] I. M. Krieger and T. J. Dougherty, A mechanism for non-Newtonian flow in suspensions of rigid spheres, *Trans. Soc. Rheol.* **3**, 137 (1959).
- [31] M. He and S. R. Nagel, Determining the refractive index, absolute thickness and local slope of a thin transparent film using multi-wavelength and multi-incident-angle interference, *Opt. Express* **28**, 24198 (2020).
- [32] C. Akcay, P. Parrein, and J. P. Rolland, Estimation of longitudinal resolution in optical coherence imaging, *Appl. Opt.* **41**, 5256 (2002).
- [33] A. Aradian, E. Raphael, and P.-G. De Gennes, “Marginal pinching” in soap films, *Europhys. Lett.* **55**, 834 (2001).
- [34] R. Braun, S. Snow, and S. Naire, Models for gravitationally-driven free-film drainage, *J. Eng. Math.* **43**, 281 (2002).
- [35] C. Breward and P. Howell, The drainage of a foam lamella, *J. Fluid Mech.* **458**, 379 (2002).
- [36] P. Howell and H. A. Stone, On the absence of marginal pinching in thin free films, *Eur. J. Appl. Math.* **16**, 569 (2005).

- [37] A. Gros, A. Bussonnière, S. Nath, and I. Cantat, Marginal regeneration in a horizontal film: Instability growth law in the nonlinear regime, [Phys. Rev. Fluids](#) **6**, 024004 (2021).
- [38] C. Trégouët and I. Cantat, Instability of the one-dimensional thickness profile at the edge of a horizontal foam film and its plateau border, [Phys. Rev. Fluids](#) **6**, 114005 (2021).
- [39] O. V. Voinov, Theory of thinning of free viscous fluid films, [J. Appl. Mech. Tech. Phys.](#) **15**, 340 (1974).
- [40] M. Le Merrer, D. Quéré, and C. Clanet, Buckling of Viscous Filaments of a Fluid under Compression Stresses, [Phys. Rev. Lett.](#) **109**, 064502 (2012).
- [41] J. Teichman and L. Mahadevan, The viscous catenary, [J. Fluid Mech.](#) **478**, 71 (2003).
- [42] A. T. Oratis, J. W. Bush, H. A. Stone, and J. C. Bird, A new wrinkle on liquid sheets: Turning the mechanism of viscous bubble collapse upside down, [Science](#) **369**, 685 (2020).
- [43] H. K. Habibi and R. Krechetnikov, Soap film catastrophes, [J. Fluid Mech.](#) **926**, A19 (2021).